Title

Hybrid metal—organic chalcogenide nanowires with electrically conductive inorganic core through diamondoid-directed assembly

Journal

Nature Materials, 16(3)

ISSN

1476-1122

Authors

Yan, Hao

Hohman, J Nathan

Li, Fei Hua

et al.

Publication Date

2017-03-01

DOI

10.1038/nmat4823

Peer reviewed

nature materials

ARTICLES

PUBLISHED ONLINE: 26 DECEMBER 2016 | DOI: 10.1038/NMAT4823

Hybrid metal–organic chalcogenide nanowires with electrically conductive inorganic core through diamondoid-directed assembly

Hao Yan[1,2†], J. Nathan Hohman[3†], Fei Hua Li[1,2†], Chunjing Jia[1], Diego Solis-Ibarra[4], Bin Wu[1,2], Jeremy E. P. Dahl[1], Robert M. K. Carlson[1], Boryslav A. Tkachenko[5], Andrey A. Fokin[5], Peter R. Schreiner[5], Arturas Vailionis[6], Taeho Roy Kim[1,2], Thomas P. Devereaux[1], Zhi-Xun Shen[1] and Nicholas A. Melosh[1,2*]

Controlling inorganic structure and dimensionality through structure-directing agents is a versatile approach for new materials synthesis that has been used extensively for metal–organic frameworks and coordination polymers. However, the lack of 'solid' inorganic cores requires charge transport through single-atom chains and/or organic groups, limiting their electronic properties. Here, we report that strongly interacting diamondoid structure-directing agents guide the growth of hybrid metal–organic chalcogenide nanowires with solid inorganic cores having three-atom cross-sections, representing the smallest possible nanowires. The strong van der Waals attraction between diamondoids overcomes steric repulsion leading to a *cis* configuration at the active growth front, enabling face-on addition of precursors for nanowire elongation. These nanowires have band-like electronic properties, low effective carrier masses and three orders-of-magnitude conductivity modulation by hole doping. This discovery highlights a previously unexplored regime of structure-directing agents compared with traditional surfactant, block copolymer or metal–organic framework linkers.

Transition metal dichalcogenides are low-dimensional systems that have attracted interest for a variety of novel physical properties, including dimensionality-modulated band structure[1], extremely weak charge screening[2] and enhanced electron–phonon coupling[3]. Recent discoveries have also shown that the bonding configuration of the metal and chalcogen in a transition metal dichalcogenide is closely correlated with the electronic properties[4]. A promising synthetic route towards precise structure and dimensionality control is bottom-up assembly using molecular structure-directing agents (SDAs). This approach guides inorganic bonding by the organic SDAs, providing a high degree of structural control through ligand selection. Metal–organic framework (MOFs)[5], coordination polymers[6], zeolites[7] and supramolecular assemblies[8] with atomically well-defined structures and tunable dimensionality are synthesized with this approach. Theoretically, this approach could be extended to create metal–organic chalcogenides (MOCs) with solid inorganic cores through appropriate selection of SDAs, tailoring their electronic properties. However, so far no SDA mechanism has been developed for highly crystalline, solid-core one-dimensional (1D) chalcogenides with band-like semiconductor properties.

A major challenge to create electrically conductive MOCs is to balance the strength of the covalently driven inorganic reactions and non-covalent interactions between ligands. In MOF-type materials, 'strong' interactions between the metal ions and organic linkers guide the assembly. In most of these materials, the metal centres are separated by the organic linkers[9], though a small group of ligand-directed metal–chalcogen atomic chains has also been identified[10]. In both cases, electrical conductivity is impaired by Peierls distortion, point defects or insulating organic molecules. On the other hand, 'weakly' interacting SDAs such as surfactants[11], peptide amphiphiles[12] or block copolymers[13] lead to solid, inorganic materials within microphase-separated regions, yet the large sizes and loss of crystallinity make this route less attractive.

Here, we demonstrate that a new class of rigid-cage SDAs with an intermediate level of non-covalent interaction strengths form highly crystalline, multi-atom cross-section inorganic cores with electrical conductivity. We chose diamondoids[14–16] as SDAs, which are atomically precise hydrogen-terminated diamond nanoparticles with intermolecular non-bonding interactions of energy scales comparable to chemical bonds[17–19]. During assembly, the diamondoids provide steric bulk and unusually strong van der Waals (vdW) attraction (London force), both of which participate in directing the inorganic cores to adopt otherwise inaccessible structures.

Optimized MOC crystal synthesis was performed at the interface between immiscible solutions of metal salts (for example, copper sulfate) and diamondoid thiols (Fig. 1a). Two types of diamondoid thiol were tested, namely adamantane-1-thiol (1AD) and diamantane-4-thiol (4DI). The synthesis yielded needle-shaped crystals (Fig. 1b) with diameters ranging from 10 nm to 20 μm, and lengths exceeding 100 μm depending on the synthetic conditions (Methods). Single-crystal X-ray diffraction (SC-XRD) revealed that the copper adamantane-1-thiolate (1ADCu) system (Fig. 1c and Supplementary Fig. 1) consists of molecular-scale core–shell nanowires (NWs) packed in a 3D supramolecular lattice. The shell is composed of closely packed adamantyl moieties

[1]Stanford Institute for Materials and Energy Sciences, Stanford, California 94305, USA. [2]Department of Materials Science and Engineering, Stanford, California 94305, USA. [3]Lawrence Berkeley National Laboratory, Berkeley, California 94720, USA. [4]Instituto de Investigaciones en Materiales, Universidad Nacional Autónoma de México, Coyoacán, CDMX 04510, México. [5]Institute of Organic Chemistry, Justus-Liebig University, Heinrich-Buff-Ring 17, D-35392 Giessen, Germany. [6]Geballe Laboratory for Advanced Materials, Stanford University, Stanford, California 94305, USA. †These authors contributed equally to this work. *e-mail: nmelosh@stanford.edu

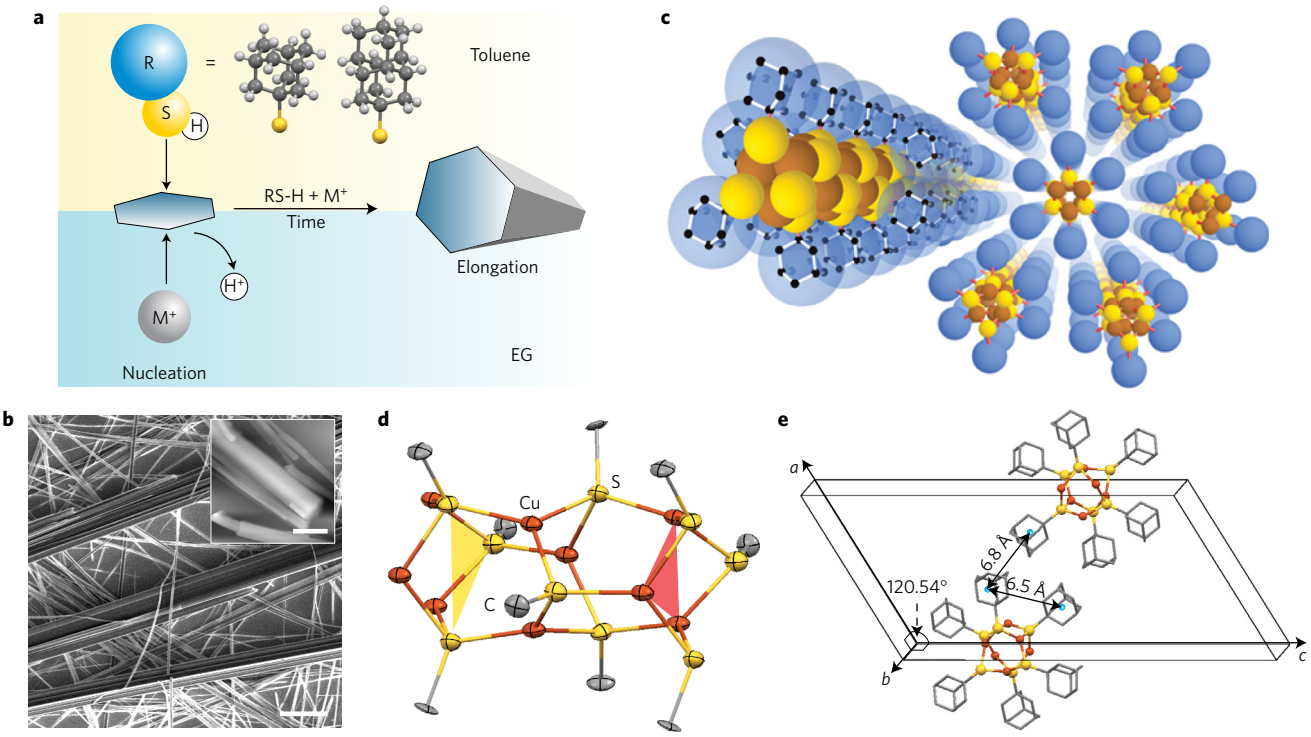

Figure 1 | Schematic of synthesis and structure of MOC crystals. a, Schematic of the two-phase synthetic strategy for MOC crystals. R, adamantane or diamantane; M, Cu; EG, ethylene glycol. **b**, Representative scanning electron microscopy (SEM) micrograph of 1ADCu crystals. Inset: atomic force microscopy (AFM) image of the 1ADCu crystals. Scale bars, 10 μm (SEM), 1 μm (AFM). **c**, Refined SC-XRD structure of 1ADCu viewed along the chain elongation direction. Cu, S and C are represented by brown, yellow and black colours, respectively. The blue spheres denote the vdW radii of the adamantane side group. **d**, Side view of individual 1ADCu NW structure solved by SC-XRD. The atoms are represented by their 50%-probability ellipsoids. Only the α-carbons in the adamantyl side groups are shown for clarity. The yellow and red triangles represent the three-atom S and Cu rings respectively. **e**, Unit cell of the 1ADCu crystal solved by SC-XRD. Cu and S atoms are represented by red and yellow spheres, and the adamantyl groups are represented by the grey capped-stick model. Hydrogen atoms are omitted for clarity. The blue dots denote the centroid of the adamantyl groups.

(blue spheres, Fig. 1c). The inorganic core consists of a cross-section of alternating three-atom Cu and S trigonal rings (yellow and red planes, Fig. 1d). Each Cu atom binds to three S atoms with a twisted trigonal planar geometry, while the S atoms are attached to three Cu atoms and its adamantyl side group in a distorted tetrahedral configuration. Finally, the 1ADCu core–shell structures pack into a distorted hexagonal lattice (Fig. 1e) with the inorganic cores elongating along the *b* axis. The average centre-to-centre distance and H···H contact distances between adamantyl moieties are 6.7 and 2.3 Å, comparable to those in adamantane crystals[20] (6.6 and 2.2 Å respectively). Furthermore, the centre-to-centre distance is close to the computed optimal distance between two adamantane molecules with minimum total energy in vacuum[21]. These observations indicate that the adamantane groups in 1ADCu are in vdW contact with their closest neighbours. The closely packed diamondoid shell gives the 1ADCu crystals remarkable stability, allowing them to be stored in air without degradation and dispersed into solvents including isopropanol and anisole without disrupting the lattice structure (Supplementary Fig. 2).

In contrast with single-atom-wide backbones found within coordination polymers, the 1ADCu has a 'solid' inorganic core consisting of a three-atom cross-section. The Cu–S core can be viewed as a nanowire with a three-atom circumference, representing the smallest conceivable solid nanowire structure. In comparison, the smallest stable carbon nanotubes have ten atoms on the circumference[22].

The three-atom cross-section in 1ADCu nanowire suggests a different nucleation and growth mechanism from coordination polymers with atomic chain backbones. Specifically, a multi-atom inorganic growth front must be formed in the nuclei and subsequently stabilized during axial elongation. To understand this process, we choose to examine the stability and extension of a cyclic trimer of copper adamantyl thiolate, representing the smallest structural repeating unit of the 1ADCu NW (Supplementary Fig. 3a). The cyclic trimer may assume either the *cis* configuration where all three adamantyl groups reside on the same side of the Cu–S plane and expose the inorganic face free of steric hindrance, or the *trans* configuration where the adamantyl groups reside on both sides of the Cu–S plane (left panels, Fig. 2). The *trans*-trimer is sterically favoured as it increases the distance between adamantyl groups.

Energy minimization of the trimer structures was performed with density functional theory (DFT) using the Perdew–Burke–Ernzerhof (PBE) exchange–correlation functional[23] and a double numeric basis set with *d*-polarization (DND)[24]. DFT computation without long-range vdW interactions shows that the *trans* conformer is 0.9 kJ mol^{-1} more stable. However, computation including vdW interactions[25] (Supplementary Information) finds that the *cis*-trimer is more stable by 5.2 kJ mol^{-1} than the *trans*-trimer. In the *cis* configuration the centroid distance and H···H contact distances are 6.6 and 2.3 Å between adamantyl groups, indicating that they are in vdW contact with each other[20,21] and thus maximizing the attractive interaction. These computational results show that the strong vdW attraction between adamantyl side groups overcomes the inherent steric repulsion, yielding a lower-energy *cis* configuration.

The *cis*-trimer opens one side of the Cu–S plane for approach and reaction of other trimers or monomers in a 'face-on' manner (blue cone, upper left panel, Fig. 2). After this initial elongation step to form copper adamantyl thiolate hexamers (right panels, Fig. 2), the system again has a choice of conformations. The

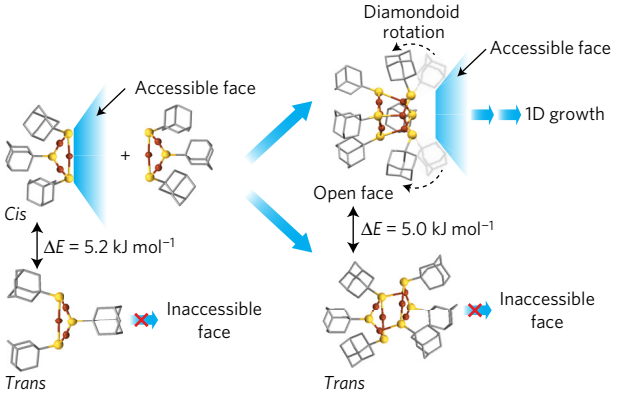

Figure 2 | 'Face-on' growth mechanism of 1ADCu. Cyclic trimers of 1ADCu prefer the *cis* arrangement of adamantyl side groups (upper left) to the *trans* configuration (bottom left) by 5.2 kJ mol^{-1}, leaving the inorganic face accessible to further addition. Subsequent formation of the hexamer reveals that despite the increased steric repulsion, the 'open-face' conformation (top right), where the three adamantyl groups rotate to be in vdW contact, is more favourable than the *trans* configuration (bottom right) by 5.0 kJ mol^{-1}, once again revealing the inorganic face and allowing NW elongation. All structures and relative energies are computed by DFT. The black double-headed arrows denote energy differences, with structures on the bottom having higher energy. The blue block arrows indicate propagation of NW growth.

adamantyl side groups in the hexamer could distribute evenly in the *trans* configuration to minimize steric repulsion (bottom right, Fig. 2), or group together, exposing the Cu–S triangular face (upper right, Fig. 2). In the hexamers the *trans* configuration is sterically favoured by 5.9 kJ mol^{-1} (Supplementary Fig. 4), deduced from DFT computation without vdW correction. However, DFT computation including vdW interactions[25] shows that the configuration where the three adamantyl groups rotate to be in vdW contact (upper right, Fig. 2) has lower energy by 5.0 kJ mol^{-1}, leaving the inorganic face open once again. This consistent energetic preference of the open-face configuration allows continuous 'face-on' addition of new precursors (ions and oligomers) and solid-core nanowire elongation. This is in contrast to the growth mechanism of previously reported coordination polymers where a single-atom growth front is present and chain elongation propagates through, for example, ring-opening or 'edge-on' polymerization[26,27].

Comparing with other 1D nanostructures such as carbon nanotubes and inorganic NWs grown by the vapour–liquid–solid mechanism, the 1ADCu NWs have atomically precise composition and diameter. To investigate why the three-atom cross-section is energetically preferred to larger diameters, we computed the optimized structures of infinitely extended copper adamantyl thiolate NWs with three, four and five sulfur atoms in the circumference (referred to as 3-, 4- and 5-atom NWs, Fig. 3a–c), as well as a planar copper adamantyl thiolate sheet (Fig. 3d). NWs of different diameters can all be mapped onto a 2D triangular tessellation of Cu and S atoms (see Methods and Supplementary Fig. 5 for more discussion). The computed 3-atom NW structure (Fig. 3a) is very close (less than 1.5% bond length and bond angle deviations) to that measured by SC-XRD (Supplementary Table 2), validating the computational method. Total energies of 4- and 5-atom NWs as well as the 2D sheet are 32.7, 72.6 and 66.2 kJ mol^{-1} higher than the 3-atom NW (right axis, Fig. 3e). The 2D sheet and 5-atom NW were not viable, instead showing large distortion and/or restructuring after geometry optimization due to the extremely small intermolecular distance in the initial structure (4.5 Å, Supplementary Fig. 5d,e). The smaller bending curvature of the larger-diameter NWs requires tighter packing of the bulky side groups, observed from the average centroid distance between adjacent adamantyl groups of 6.6, 6.0, 6.2 and 5.8 Å in the 3-, 4- and 5-atom NWs and 2D sheet respectively (right axis, Fig. 3e). Previous computations have shown that the optimal distance between adamantane molecules is ~6.7 Å, and the total energy increases by 28 kJ mol^{-1} as the distance is decreased by 1 Å due to steric repulsion[21]. In this case, the larger-diameter NW structures are less sterically favourable. In comparison, the computed geometries of copper *n*-decane-1-thiolate (C10Cu) and copper benzenethiolate (PhCu) both result in 2D sheets[28,29], consistent with their less bulky side groups (Supplementary Fig. 6). These results indicate that the steric repulsion of the large diamondoid side groups demands a large curvature of the Cu–S core, and thus determines the diameter of the 1ADCu NW.

The individual NWs are stabilized in the bulk crystal by binding together in a distorted hexagonal array. The centroid distance and H···H contact distance between adamantyl groups in adjacent NWs are 6.8 and 2.3 Å respectively, indicating that the diamondoid shells are in vdW contact[20,21]. The total energy of the 3D NW array is 50 kJ mol^{-1} lower than that of the individual NWs (blue, Fig. 3e). Roughly 80% of this energy difference originates from vdW attractions between adjacent NWs (Methods). The inter-wire vdW interaction thus further stabilizes the ultrathin 1ADCu NWs leading to crystals with sizes up to 100 μm (Fig. 1b).

Analysis of the 1ADCu system indicates that repulsion between sterically bulky side groups favours the formation of small-diameter, 3-atom NWs, while strong vdW attraction enables the face-on growth of the solid inorganic cores. To further test this concept, we evaluated a similar growth pathway for a larger diamondoid ligand, 4DI. The diamantyl side group adds an additional ~3-Å-tall isobutane cage to the length of the diamondoid compared with adamantane. DFT computation of cyclic trimers and hexamers (Fig. 4a) found that the copper diamantyl thiolate trimer also prefers the *cis* arrangement of the three diamantyl groups over the *trans* configuration, with energy difference of 4.9 kJ mol^{-1} (left panel, Fig. 4a). This would allow the face-on addition of precursors and/or oligomers, the same as in 1ADCu. However, in the hexamer structure the *trans* configuration, in which the six diamantyl groups point to two opposite directions, is 5.3 kJ mol^{-1} more stable than the open-face configuration (right panel, Fig. 3a). Thus, in the *trans*-hexamer the face-on growth front is sterically hindered by the diamantyl groups, terminating the growth. These computational results predict that while the copper diamantane-4-thiolate (4DICu) system should grow into a 1D structure, it cannot form the same three-atom inorganic cross-section as in 1ADCu, and more likely proceeds through edge-on or ring-opening growth[26,27].

We then grew the 4DICu crystal, and the SC-XRD crystal structure shows that these materials have a 3D supramolecular lattice formed by stacking 1D copper thiolate chains (Fig. 4b and Supplementary Fig. 1), similar to that of 1ADCu. However, rather than the solid-core NW seen in 1ADCu, the diamantane SDAs give rise to two Cu–S atomic chains linked into nanoribbons (NRs) surrounded by diamantyl groups (Fig. 4c), consistent with the prediction. Each NR is two atoms wide, with the edges consisting of alternating Cu and S atoms. Two types of chemical environment exist for both atoms: S takes both tetrahedral (S1) and trigonal pyramidal (S2) configurations, while Cu takes linear (Cu1) and twisted trigonal planar (Cu2) configurations. It should be emphasized that the change of Cu–S bonding configuration happens without the change of inorganic composition, and is solely the result of side-group difference. The NR growth may have propagated by adding precursors and/or oligomers to a two-atom-wide Cu–S growth front. This 'edge-on' growth mode, determined by the larger steric repulsion between diamantyl groups, is clearly different from the 'face-on' growth in 1ADCu and highlights the importance of balancing attractive and repulsive forces between diamondoid SDAs to achieve the desired growth modes.

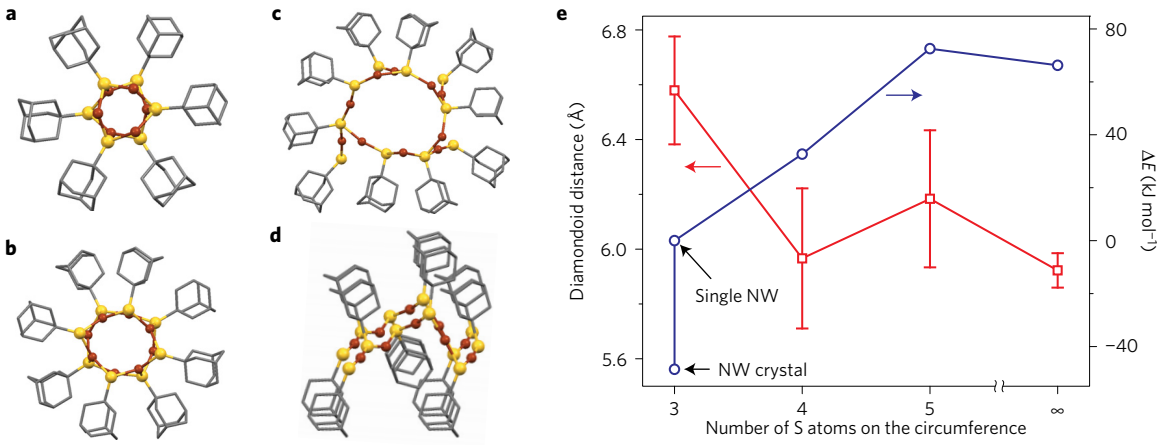

Figure 3 | Relative stabilities of 1ADCu NWs with different diameters. a–d, DFT-computed structures of 1ADCu NWs with 3 (**a**), 4 (**b**) and 5 (**c**) S atoms on the circumference, as well as 1ADCu single-layer sheet (**d**). **e**, Distance between the centroids of adjacent adamantyl side groups (left axis, red) and the relative change of total energy (right axis, blue) for the structures shown in **a–d**.

The different sizes/shapes of the SDA in 1ADCu and 4DICu systems also give rise to different inter-wire/ribbon interactions, modifying their 3D packing. Unlike the distorted hexagonal packing seen in 1ADCu, in 4DICu the individual NRs packs into a 3D cross-motif lattice (Fig. 4d), in which the diamantyl groups in adjacent chains pair up such that the long axes of the molecules are parallel or perpendicular to their nearest neighbours (red arrows, Fig. 4d). DFT computations (Supplementary Fig. 8) showed that the cross-motif pattern lowered the total energy of the system by 77 kJ mol^{-1}, indicating an inter-chain interaction energy 40% larger than that in 1ADCu (Fig. 3e) and further stabilizing the atomically thin NR structure.

The diamondoid-directed MOCs with solid inorganic cores represent a new class of chalcogenides with atomically well-defined structures, ultrasmall dimensions and unconventional bonding configurations. The continuous inorganic core with finite-sized cross-section give rise to strong energy–momentum (E–k) dispersion and thus smaller effective masses for charge carriers, unlike MOFs in which electron transport is dominated by a site hopping mechanism[30]. To this end, we first performed DFT computations of the band structures of 1ADCu and 4DICu using a plane-wave basis set and the PBE exchange–correlation functional[23] (left panels, Fig. 5a,b). Both structures show large band dispersion along the chain elongation directions (right panels, Fig. 5a,b). For example, the width of the first valence band in 1ADCu is 0.62 eV, substantially larger than those in 1D coordination polymers and 3D MOFs (Supplementary Table 3). The valence band maximum (VBM) and conduction band minimum (CBM) appear along the G–Y direction in k-space. The effective masses (m^*) of hole (h^+) and electron (e^-) carriers at the VBM and CBM are close to one electron rest mass (m_0), except for the hole carrier in 4DICu, which is close to $3m_0$ (Fig. 5c). These MOC effective carrier masses are comparable to those in inorganic chalcogenides[31]. Notably, both the highest occupied molecular orbital (HOMO, lower panel, Fig. 5d) and lowest unoccupied molecular orbital (LUMO, upper panel, Fig. 5d) of 1ADCu are located on the inorganic atoms and surrounded by the diamondoid shell. This is in contrast to the π–d conjugated coordination polymers where both the organic and inorganic components contribute to the bands near the Fermi level. The band structures between G and Y points in the k-space are further computed using the more accurate, Heyd–Scuseria–Ernzerhof (HSE) hybrid functional[32] (middle panels, Fig. 5a,b). The bandgaps predicted by these computations are 2.79 and 3.62 eV for 1ADCu and 4DICu, respectively. The computed bandgaps are in reasonable agreement with the optical bandgap for 1ADCu (2.5 eV)

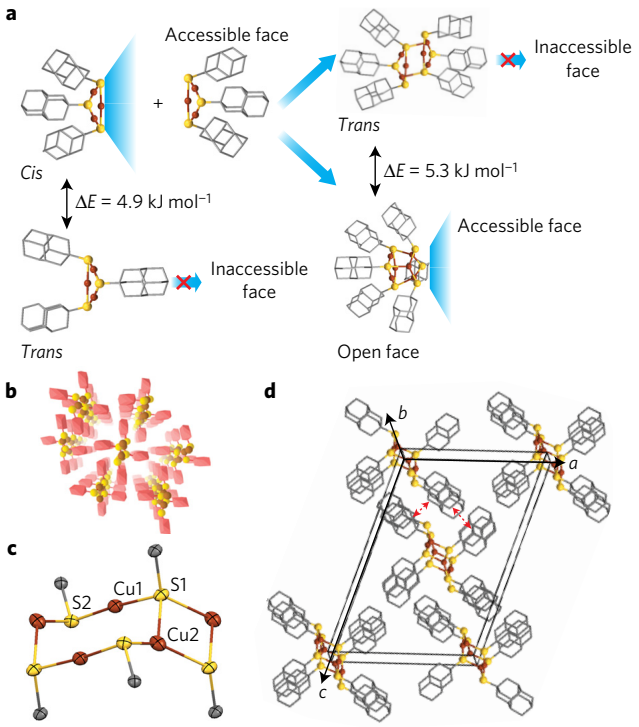

Figure 4 | Prediction of growth mode and crystal structure of 4DICu. **a**, Similar to 1ADCu, *cis* 4DICu cyclic trimers (top left) are lower in energy than the *trans* conformer (bottom left) by 4.9 kJ mol^{-1}, allowing precursor addition to the inorganic face. However, the *trans* conformation (top right) dominates over the 'open-face' conformation (bottom right) in the hexamers due to steric repulsion, preventing face-on growth. Black double-headed arrows denote energy comparison with the structures on the bottom having higher energy. Blue block arrows indicate propagation of NR growth. **b**, SC-XRD-determined atomic structure of 4DICu viewed along the chain elongation direction. The diamantyl groups are represented by their vdW spheres (red). **c**, Side view of the individual 4DICu NR structure resolved by SC-XRD. Atoms are represented by their 50%-probability ellipsoids. Only the α-carbons in the diamantyl side groups are shown for clarity. **d**, Unit cell of 4DICu determined by SC-XRD. Cu and S atoms are represented by red and yellow spheres, and the diamantyl groups are represented by the grey capped-stick model. The red dashed arrows indicate the parallel or perpendicularly paired diamantyl groups in adjacent NRs.

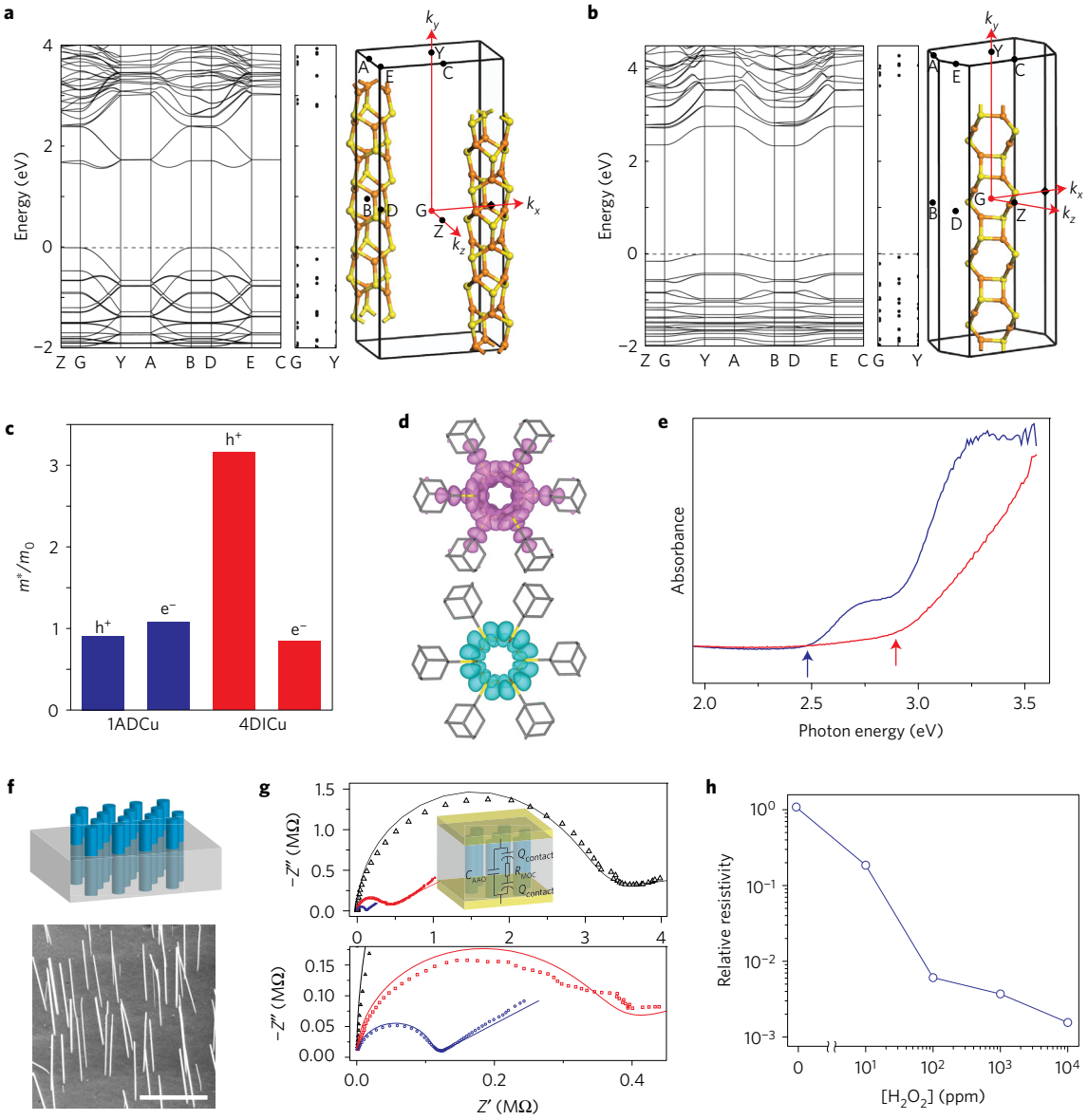

Figure 5 | Theoretical and experimental investigation of electronic properties. a,**b**, Computed band structures of 1ADCu (**a**) and 4DICu (**b**) at the PBE and HSE levels of DFT with a plane-wave basis set. The left panels show the band structures along the high-symmetry directions computed at the PBE level. The middle panels show the band structures near the VBM and CBM, computed at the HSE level. The right panels show the first Brillouin zones with the corresponding atomic structures overlaid. **c**, Effective carrier masses (in the unit of electron rest mass) near the VBM (h^+) and CBM (e^-) for 1ADCu (blue) and 4DICu (red). **d**, Spatial distributions of HOMO (green, lower panel) and LUMO (red, upper panel) in 1ADCu NW. **e**, Optical absorbance spectra of 1ADCu (blue) and 4DICu (red). The arrows denote the onset positions of the optical absorption. **f**, Schematic (upper panel) and SEM image (low panel) of vertically aligned 1ADCu crystal arrays. The 1ADCu crystal and the AAO matrix are represented by blue and grey colours respectively. Scale bar, 10 μm. **g**, Nyquist plots from vertical arrays of 1ADCu (blue), 4DICu (red) and blank AAO template (black). The discrete markers and continuous lines denote the experimental data and fitting, respectively. Inset, schematic device structure and equivalent circuit. The lower panel shows the zoom-in view of the low-impedance regime of the upper panel. **h**, Relative resistivity change of 1ADCu as a function of the concentration of H_2O_2 solution.

and 4DICu (2.9 eV) as measured by ultraviolet–visible absorption spectroscopy (Fig. 5e). Pure diamondoids have no detectable absorption in the wavelength range of 200–1,000 nm, with >6 eV bandgaps[33,34]. The 0.4 eV difference in the optical bandgaps between 1ADCu and 4DICu demonstrates bandgap modulation induced by the different non-bonding interactions between diamondoid SDAs.

The solid inorganic cores and relatively small carrier masses in the MOCs differentiate these from conductive MOFs where electrons transport by hopping or through hybrid π–d orbitals formed between metal and aromatic linkers[30,35,36]. To measure electronic transport properties, we grew vertically aligned MOC crystal arrays embedded in anodized aluminium oxide (AAO) matrices (Fig. 5f). Metal electrodes were deposited on both ends of the crystal array to measure their transport in the axial direction. Due to confinement of the HOMO and LUMO within the insulating diamondoid shells, the majority of electronic transport should occur within single wires, with a low probability of charge hopping between adjacent NWs. Nyquist impedance plots of intrinsic 1ADCu NWs in the frequency range of 1 Hz to 1 MHz (blue, Fig. 5g) fit best to an equivalent circuit consisting of a resistor (R_{MOC}), a constant-phase element ($Q_{contact}$) and a capacitor (C_{AAO}) (inset, Fig. 5g). We attribute R_{MOC}, $Q_{contact}$ and C_{AAO} to the resistance of the nanowires, the contact barrier and the capacitance of the alumina matrix, respectively. Compared with blank AAO templates

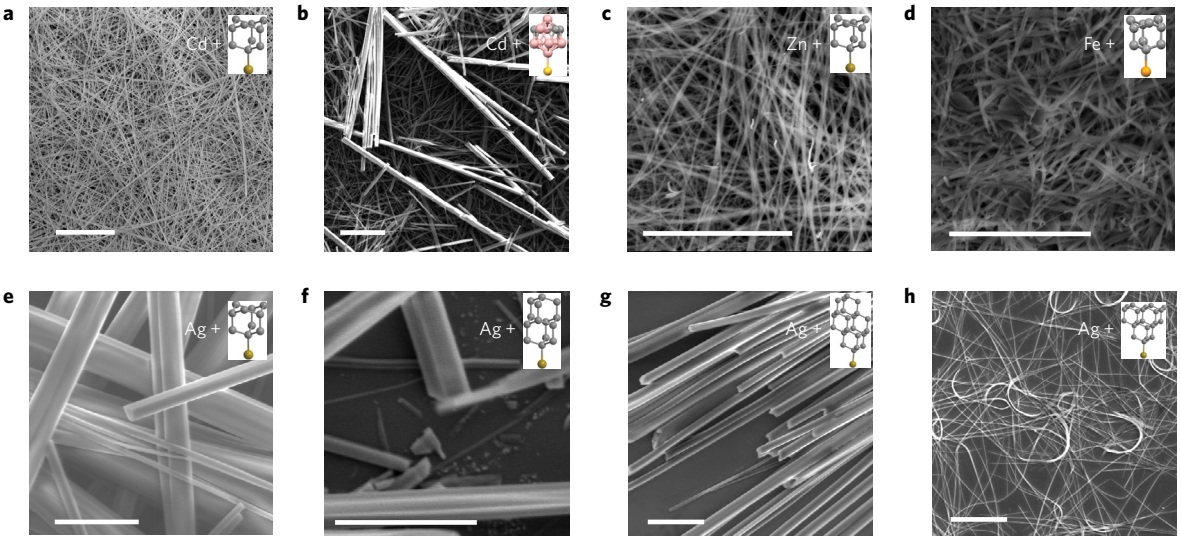

Figure 6 | SEM micrographs of MOC crystals beyond copper thiolates. a–d, MOC crystals with different metal cations: cadmium adamantane-1-thiolate (**a**), cadmium *m*-carborane-9-thiolate (**b**), zinc adamantane-1-thiolate (**c**) and iron(II) adamantane-1-selenolate (**d**). **e–h**, Ag-based MOCs with different SDA ligands: adamantane-1-thiol (**e**), diamantane-4-thiol (**f**), [121]tetramantane-6-thiol (**g**) and [1(2)3]tetramantane-3-thiol (**h**). The insets show the structures of the SDAs. Scale bars, 10 μm for **a** and **b**, and 5 μm for the rest.

without 1ADCu (black, Fig. 5g), $R_{MOC} = 0.3\,M\Omega$ was one order of magnitude lower impedance. Considering the geometry of the device and the filling ratio of the crystals in the alumina matrix (Methods), the resistivity of the 1ADCu nanowire was determined to be ∼100 Ω m, comparable to that of intrinsic silicon. 4DICu showed similar results (red, Fig. 5g) with slightly larger resistivity (∼300 Ω m). The difference is attributed to the higher effective hole mass or structural defects in the 4DICu NRs.

If MOCs have band-like electronic behaviour, their resistivity should be modulated by doping. To test the effect of doping in the MOC system, the as-synthesized 1ADCu crystals were exposed to H_2O_2 solutions with different concentrations at room temperature. The treatment partially oxidized the copper in 1ADCu from the +1 to the +2 state, as detected by X-ray photoelectron spectroscopy (Supplementary Fig. 9a) with no change in the lattice spacing as determined by XRD (Supplementary Fig. 9b). a.c. impedance measurement on powder samples showed that the doping decreased the resistivity of 1ADCu by approximately three orders of magnitude (Fig. 5h and Supplementary Fig. 10) as the H_2O_2 concentration was increased up to 10^4 ppm. Further increase of the H_2O_2 concentration disrupted the lattice (Supplementary Fig. 9b) and decreased the conductivity (Supplementary Fig. 10b,c). These results indicate that the enhanced electrical conductivity of 1ADCu originates from additional holes moving in the continuous Cu–S core. This is in contrast to enhanced transport in MOFs where molecular bridges provide alternate charge hopping paths between discrete Cu–O centres[30].

The methodology of diamondoid-directed assembly can be extended to a wide variety of low-dimensional chalcogenide materials by harnessing well-established metal–chalcogen chemistry[37]. We first demonstrate the generality of this approach via the synthesis of 1D MOC crystals with inorganic cores of Cd–S, Zn–S and Fe–Se, using adamantane as the SDA (Fig. 6a,c,d). These materials cover a broad range of potential functionalities including optoelectronics (CdS)[38], piezoelectrics (ZnS)[39] and superconductivity (FeSe)[3]. Secondly, the size and shape of the diamondoid tunes the vdW and steric interactions, modulating the inorganic bonding beyond 1AD and 4DI systems. To this end, we have synthesized silver thiolate MOCs with adamantane, diamantane and tetramantane as the SDAs. These materials show 1D morphologies (Fig. 6e–h) similar to the copper-based MOCs, yet have different crystalline structures as revealed by powder XRD (Supplementary Fig. 11). The morphology of these materials was tunable by solvent composition, with addition of ethanol to toluene generating thinner diameter 1D crystals (Supplementary Fig. 12). Lastly, we extended the choice of strongly interacting SDAs to other rigid-cage molecules such as carboranes. As a first demonstration, we synthesized cadmium *m*-carborane-9-thiolate 1D crystals (Fig. 6b), which show similar morphology to the diamondoid-directed MOCs.

The use of sterically bulky, yet strongly interacting SDAs is an intriguing avenue for synthesis of a wide variety of low-dimensional materials that retain band-like transport. The strongly confined, diamondoid-insulated inorganic cores present a promising area for interesting physics such as strong electron–electron[40] and electron–phonon coupling[41,42]. Moreover, the new regime of structure-directing mechanism can be extended to other systems such as $MoSe_2$ and Bi_2Se_3. Controlling dimensionality and bonding configuration in these materials via the choice of diamondoid (and other cage-like molecule) SDAs provides a general approach to tune their electronic properties and access new materials and structures.

Methods

Methods, including statements of data availability and any associated accession codes and references, are available in the online version of this paper.

Received 11 February 2016; accepted 14 November 2016; published online 26 December 2016

References

1. Zhang, Y. *et al*. Direct observation of the transition from indirect to direct bandgap in atomically thin epitaxial $MoSe_2$. *Nat. Nanotech.* **9,** 111–115 (2014).
2. Ugeda, M. M. *et al*. Giant bandgap renormalization and excitonic effects in a monolayer transition metal dichalcogenide semiconductor. *Nat. Mater.* **13,** 1091–1095 (2014).
3. Lee, J. J. *et al*. Interfacial mode coupling as the origin of the enhancement of T_c in FeSe films on $SrTiO_3$. *Nature* **515,** 245–248 (2014).
4. Kappera, R. *et al*. Phase-engineered low-resistance contacts for ultrathin MoS_2 transistors. *Nat. Mater.* **13,** 1128–1134 (2014).
5. Yaghi, O. M. *et al*. Reticular synthesis and the design of new materials. *Nature* **423,** 705–714 (2003).
6. Leong, W. L. & Vittal, J. J. One-dimensional coordination polymers: complexity and diversity in structures, properties, and applications. *Chem. Rev.* **111,** 688–764 (2011).

7. Simancas, R. *et al*. Modular organic structure-directing agents for the synthesis of zeolites. *Science* **330,** 1219–1222 (2010).
8. Chakrabarty, R., Mukherjee, P. S. & Stang, P. J. Supramolecular coordination: self-assembly of finite two- and three-dimensional ensembles. *Chem. Rev.* **111,** 6810–6918 (2011).
9. Furukawa, H. *et al*. The chemistry and applications of metal–organic frameworks. *Science* **341,** 1230444 (2013).
10. Su, W. *et al*. Tunable polymerization of silver complexes with organosulfur ligand: counterions effect, solvent- and temperature-dependence in the formation of silver(I)-thiolate(and/or thione) complexes. *Inorg. Chim. Acta* **331,** 8–15 (2002).
11. Fan, H. Nanocrystal-micelle: synthesis, self-assembly and application. *Chem. Commun.* 1383–1394 (2008).
12. Cui, H., Webber, M. J. & Stupp, S. I. Self-assembly of peptide amphiphiles: from molecules to nanostructures to biomaterials. *Biopolymers* **94,** 1–18 (2010).
13. Zhao, D. Triblock copolymer syntheses of mesoporous silica with periodic 50 to 300 Ångstrom pores. *Science* **279,** 548–552 (1998).
14. Dahl, J. E., Liu, S. G. & Carlson, R. M. K. Isolation and structure of higher diamondoids, nanometer-sized diamond molecules. *Science* **299,** 96–99 (2003).
15. Schwertfeger, H., Fokin, A. A. & Schreiner, P. R. Diamonds are a chemist's best friend: diamondoid chemistry beyond adamantane. *Angew. Chem. Int. Ed.* **47,** 1022–1036 (2008).
16. Gunawan, M. A. *et al*. Diamondoids: functionalization and subsequent applications of perfectly defined molecular cage hydrocarbons. *New J. Chem.* **38,** 28–41 (2014).
17. Schreiner, P. R. *et al*. Overcoming lability of extremely long alkane carbon–carbon bonds through dispersion forces. *Nature* **477,** 308–311 (2011).
18. Fokin, A. A. *et al*. Stable alkanes containing very long carbon–carbon bonds. *J. Am. Chem. Soc.* **134,** 13641–13650 (2012).
19. Wagner, J. P. & Schreiner, P. R. London dispersion in molecular chemistry-reconsidering steric effects. *Angew. Chem. Int. Ed.* **54,** 12274–12296 (2015).
20. Nowacki, W. Die Krystallstruktur von Adamantan (symm. Tri-cyclo-decan). *Helv. Chim. Acta* **28,** 1233–1242 (1945).
21. Makowski, M., Czaplewski, C., Liwo, A. & Scheraga, H. A. Potential of mean force of association of large hydrophobic particles: toward the nanoscale limit. *J. Phys. Chem. B* **114,** 993–1003 (2010).
22. Wang, N., Tang, Z. K., Li, G. D. & Chen, J. S. Single-walled 4 Å carbon nanotube arrays. *Nature* **408,** 50–51 (2000).
23. Perdew, J. P., Burke, K. & Ernzerhof, M. Generalized gradient approximation made simple. *Phys. Rev. Lett.* **77,** 3865–3868 (1996).
24. Delley, B. An all-electron numerical method for solving the local density functional for polyatomic molecules. *J. Chem. Phys.* **92,** 508–517 (1990).
25. Tkatchenko, A. & Scheffler, M. Accurate molecular van der Waals interactions from ground-state electron density and free-atom reference data. *Phys. Rev. Lett.* **102,** 73005 (2009).
26. Lozano, E., Nieuwenhuyzen, M. & James, S. L. Ring-opening polymerisation of silver–diphosphine $[M_2L_3]$ coordination cages to give $[M_2L_3]$ coordination polymers. *Chem. Eur. J.* **7,** 2644–2651 (2001).
27. Jiang, J.-J. *et al*. Structural disorder and transformation in crystal growth: direct observation of ring-opening isomerization in a metal–organic solid solution. *IUCrJ* **1,** 318–327 (2014).
28. Espinet, P., Lequerica, M. C. & Martín-Alvarez, J. M. Synthesis, structural characterization and mesogenic behavior of copper(I) *n*-alkylthiolates. *Chem. Eur. J.* **5,** 1982–1986 (1999).
29. Low, K.-H., Roy, V. A. L., Chui, S. S.-Y., Chan, S. L.-F. & Che, C.-M. Highly conducting two-dimensional copper(I) 4-hydroxythiophenolate network. *Chem. Commun.* **46,** 7328–7330 (2010).
30. Talin, A. A. *et al*. Tunable electrical conductivity in metal–organic framework thin-film devices. *Science* **343,** 66–69 (2014).
31. Yu, S., Xiong, H. D., Eshun, K., Yuan, H. & Li, Q. Phase transition, effective mass and carrier mobility of MoS_2 monolayer under tensile strain. *Appl. Surf. Sci.* **325,** 27–32 (2015).
32. Krukau, A. V., Vydrov, O. A., Izmaylov, A. F. & Scuseria, G. E. Influence of the exchange screening parameter on the performance of screened hybrid functionals. *J. Chem. Phys.* **125,** 224106 (2006).
33. Raty, J.-Y., Galli, G., Bostedt, C., Van Buuren, T. W. & Terminello, L. J. Quantum confinement and fullerenelike surface reconstructions in nanodiamonds. *Phys. Rev. Lett.* **90,** 37401 (2003).
34. Richter, R. *et al*. Size and shape dependent photoluminescence and excited state decay rates of diamondoids. *Phys. Chem. Chem. Phys.* **16,** 3070–3076 (2014).
35. Sheberla, D. *et al*. High electrical conductivity in Ni_3(2,3,6,7,10,11-hexaiminotriphenylene)$_2$, a semiconducting metal–organic graphene analogue. *J. Am. Chem. Soc.* **136,** 8859–8862 (2014).
36. Huang, X. *et al*. A two-dimensional π–d conjugated coordination polymer with extremely high electrical conductivity and ambipolar transport behaviour. *Nat. Commun.* **6,** 7408 (2015).
37. Gimeno, M. C. & Gimeno, M. C. *Handbook of Chalcogen Chemistry* 33–80 (Royal Society of Chemistry, 2006).
38. Agarwal, R., Barrelet, C. J. & Lieber, C. M. Lasing in single cadmium sulfide nanowire optical cavities. *Nano Lett.* **5,** 917–920 (2005).
39. Lu, M.-Y. *et al*. ZnO—ZnS heterojunction and ZnS nanowire arrays for electricity generation. *ACS Nano* **3,** 357–362 (2009).
40. Voit, J. One-dimensional Fermi liquids. *Rep. Prog. Phys.* **58,** 977–1116 (1995).
41. Yang, W. L. *et al*. Monochromatic electron photoemission from diamondoid monolayers. *Science* **316,** 1460–1462 (2007).
42. Clay, W. A. *et al*. Origin of the monochromatic photoemission peak in diamondoid monolayers. *Nano Lett.* **9,** 57–61 (2009).

Acknowledgements

The authors thank M. Soltis and I. Mathews at SLAC National Accelerator Laboratory and S. Teat at Lawrence Berkeley National Laboratory for assistance with SC-XRD, and Y. Liang at Lawrence Berkeley National Laboratory for help with DFT computations. Part of this work was performed at the Stanford Nano Shared Facilities (SNSF). This work was supported by the Department of Energy, Office of Basic Energy Sciences, Division of Materials Science and Engineering, under contract DE-AC02-76SF00515. The work done at the Justus-Liebig University was further supported by the Deutsche Forschungsgemeinschaft, Priority Program 'Dispersion' (SPP 1807, Schr 597/27-1). Portions of this research were carried out at the Stanford Synchrotron Radiation Lightsource (SSRL), a Directorate of SLAC National Accelerator Laboratory and an Office of Science User Facility operated for the US Department of Energy Office of Science by Stanford University. The SSRL Structural Molecular Biology Program is supported by the DOE Office of Biological and Environmental Research, and by the National Institutes of Health, National Institute of General Medical Sciences (including P41GM103393). The contents of this publication are solely the responsibility of the authors and do not necessarily represent the official views of NIGMS or NIH. This research used resources of the National Energy Research Scientific Computing Center (NERSC) and Advanced Light Source (ALS), both of which are DOE Office of Science User Facilities supported by the Office of Science of the US Department of Energy under Contract No. DE-AC02-05CH11231.

Author contributions

H.Y., J.N.H., Z.-X.S., P.R.S. and N.A.M. conceived the idea. H.Y., J.N.H., F.H.L., B.W. and T.R.K. performed the growth experiments and the physical measurements. H.Y., F.H.L., C.J. and T.P.D. performed the DFT computations. D.S.-I. and A.V. solved the crystal structures from SC-XRD data. J.E.P.D., R.M.K.C., B.A.T., A.A.F. and P.R.S. provided the diamondoids and synthesized their derivatives. H.Y., J.N.H. and N.A.M. wrote the paper. All authors contributed to the discussion and revision of the paper.

Additional information

Supplementary information is available in the online version of the paper. Reprints and permissions information is available online at www.nature.com/reprints. Correspondence and requests for materials should be addressed to N.A.M.

Competing financial interests

The authors declare no competing financial interests.

Methods

Synthesis. Toluene, ethylene glycol (EG), ethanol, isopropanol (IPA), acetonitrile, *n*-octane, adamantane-1-thiol, *m*-carborane-9-thiol, copper(II) sulfate ($CuSO_4$), silver nitrate ($AgNO_3$), cadmium sulfate ($CdSO_4$), zinc sulfate ($ZnSO_4$), iron(II) chloride ($FeCl_2$), tributylphosphine (TBP) and hydrogen peroxide (H_2O_2, 30% aqueous solution) were used as received from Sigma-Aldrich. Anhydrous/dry reagents were used when possible. Diamantane-4-thiol, [121]tetramantane-6-thiol, [1(2)3]tetramantane-3-thiol and adamantane-1-selenol were prepared as described previously[43,44]. Water was purified with a Milli-Q Gradient system (EMD Millipore). All crystals were synthesized in air except iron(II) adamantane-1-selenolate, which was prepared in an argon-filled glove box with <0.5 ppm oxygen and water levels.

For synthesis of copper-based MOCs, anhydrous $CuSO_4$ and diamondoidthiol were first dissolved in EG and toluene respectively, at 20 mM concentration. The dissolution of $CuSO_4$ took place at 80 °C over a period of 24 h, resulting in a light-blue solution. The solutions were then carefully layered in a borosilicate scintillation vial (Thermo Fisher Scientific) with the EG phase at the bottom. Crystals nucleated at the interface immediately, and were left to grow for >24 h at 80 °C. Copper was reduced from the (+2) to the (+1) oxidation state, observed via X-ray photoelectron spectroscopy (Supplementary Fig. 9), probably during the dissolution of $CuSO_4$ in EG, or reaction with the thiols[45,46]. The products were isolated by vacuum filtration over P4 filter paper (Thermo Fisher Scientific), rinsed with ethanol to remove residual solvent and thoroughly dried under vacuum at room temperature.

For synthesis of silver-based MOCs, a similar procedure as used for copper-based MOCs was adopted, except that $AgNO_3$ was dissolved in water instead of EG at 20 mM concentration.

For synthesis of cadmium-based MOCs, a similar procedure as used for copper-based MOCs was adopted. For the synthesis of cadmium *m*-carborane-9-thiolate, the carborane thiol was dissolved in toluene at 20 mM concentration. Saturated $CdSO_4$ solution in EG with some solid at the bottom was used due to the low solubility of $CdSO_4$. After the synthesis, un-reacted $CdSO_4$ solid was carefully removed using a pipette before the crystals on the toluene/EG interface were harvested.

For synthesis of zinc adamantane-1-thiolate, a similar procedure as used for copper-based MOCs was adopted. $ZnSO_4$ was dissolved in EG at 20 mM concentration. Crystals were allowed to grow for a month before harvest.

For synthesis of iron(II) adamantane-1-selenolate, all operations were performed in an argon-filled glove box. Anhydrous $FeCl_2$ and adamantane-1-selenol were dissolved in acetonitrile and *n*-octane, respectively, at 20 mM concentration. The dissolution of $FeCl_2$ took place at 40–50 °C over the course of 1–2 days. Five millilitres of the two solutions were then carefully layered with the acetonitrile phase at the bottom. Addition of 1 ml TBP to the layered 2-phase solutions resulted in immediate colour change at the interface to yellow, which then spread to both phases. TBP has been reported to facilitate the formation of Fe–Se bonds without incorporation into the crystal structure[47]. Formation of iron(II) adamantane-1-selenolate crystals at the interface took place at 40–50 °C over the course of 1–2 weeks. The resulting crystals were collected by filtration through a polytetrafluoroethylene membrane (FGLP04700, EMD Millipore) or by centrifugation at 12,000 rounds per minute (r.p.m.). Control reactions between TBP and adamantane-1-selenol or $FeCl_2$ yielded no product.

For the growth of vertical MOC arrays (Fig. 5f), an AAO membrane with 200 nm pore size and 60 μm thickness (Anodisc 13, Whatman) was placed at the toluene/EG interface. Growth was performed under the same conditions as above. After the growth the membrane was gently rinsed with toluene and IPA, and dried in a carbon dioxide critical point dryer (Autosamdri-815, Tousimis).

To dope the MOCs, H_2O_2 was first diluted with IPA to 10, 100, 1,000 and 10,000 ppm concentrations. MOC powders were immersed in the solution with stirring at room temperature for 30 min before vacuum filtration, rinsing and vacuum drying. We note that H_2O_2 has been used as an oxidative doping reagent for conductive polymers[48].

XRD structural determination. For SC-XRD measurements, the as-synthesized crystals were carefully lifted out of the solvent, coated with Paratone-N oil and attached to a Kapton loop. SC-XRD data for 1ADCu were obtained at Beamline 11.3.1, ALS, Lawrence Berkeley National Laboratory, equipped with a Bruker D8 diffractometer and a Bruker AXS APEX II CCD detector. SC-XRD of 4DICu was performed at Beamline 12.2, SSRL, SLAC National Accelerator Laboratory, equipped with a Dectris Pilatus 6M detector. Frames were collected using ω and/or ψ scans and the unit-cell parameters were refined against all data. Data were integrated and corrected for Lorentz and polarization factors, as well as the absorption effects, by either SAINT 8.27b and SADABS V2012 or XDS[49,50]. Space-group assignments were based on systematic absences, *E*-statistics, agreement factors for equivalent reflections, and successful refinement of the structure. The structures were solved by direct methods and expanded through successive difference Fourier maps using SHELXS-97. They were refined against all data using SHELXTL and OLEX2 software[51–54]. Hydrogen atoms were inserted at idealized positions and refined using an isotropic thermal parameter 1.2 times that of the attached atom. All non-hydrogen atoms were refined anisotropically. Details regarding the data quality and a summary of the residual values of the refinements are listed in Supplementary Table 1.

In the crystal structure of 4DICu, void regions in the asymmetric unit (203 $Å^3$ and 203 $Å^3$ located at coordinates 0.000, 0.545, 0.500 and 0.500, 0.575, 1.000 respectively) contain disordered toluene molecules. A solvent mask was used to remove the scattering contribution of these solvent-correlated electron densities from the diffraction data using OLEX2. The mask removed the equivalent of 98 electrons per unit cell[53].

Powder XRD of 1ADCu (Supplementary Fig. 9b) was measured on a D8 Venture diffractometer (Bruker AXS) with a Cu Kα source (wavelength: 1.541 Å) and a Photon 100 CMOS detector. Powder samples were loaded in borosilicate capillary tubes (Charles Supper) and measured with the Debye–Scherrer geometry at room temperature.

***In silico* construction of atomic structural models.** The initial structure of the 1ADCu *cis*-trimer (Supplementary Fig. 3a) was obtained by 'cropping' the chemical repeating unit of 1ADCu NW, consisting of three copper cations and three adamantyl thiolate anions, out of the infinitely extended 1D structure. Similarly, the initial structure of the 'open-face' hexamer (Supplementary Fig. 3c) was obtained by cropping out two chemical repeating units from the 1D NW. To obtain the *trans*-trimer (Supplementary Fig. 3b) and *trans*-hexamer (Supplementary Fig. 3d), one or three of the adamantyl groups were manually flipped to the opposite side of the Cu–S triangular plane. The initial structures of 4DICu trimers and hexamers (Supplementary Fig. 7) were obtained by substituting adamantyl with diamantyl.

Atomic models of the 1ADCu NWs with different diameters (Supplementary Fig. 5b–d) were built by modifying boron nitride nanotubes with the same chiral indices (see Supplementary Information). The atomic model of the 1ADCu 2D sheet (Supplementary Fig. 5e) was constructed by modifying a hexagonal boron nitride monolayer. The B and N atoms were replaced with Cu and S, and the diamondoid side groups were attached to the S. For the 2D sheet, the adamantyl groups were arranged evenly on both sides of the sheet. The initial Cu–S bond lengths were set to 2.2–2.3 Å for the NWs and 2.6 Å for the 2D sheet, to avoid overlapping between adjacent adamantyl groups.

To compute the optimized geometries and total energies of individual 1ADCu NWs (Fig. 3) and 4DICu NRs (Supplementary Fig. 8a), a single NW/NR was placed in an arbitrary tetragonal lattice such that the distance between diamondoids in adjacent chains was larger than 15 Å. Previous computations on adamantane and related molecules[21] have shown that the vdW energy between molecules at this distance is small, such that each MOC NW/NR behaves as it would in isolation.

DFT computations. All atomic structure and energy computations were performed using the DMol^3 program in the Materials Studio 8.0 (BIOVIA) suite. We chose this program for its balanced speed and accuracy in handling both molecular and periodic systems. DFT computations were performed with the PBE exchange–correlation functional[23] and the DND basis set[24]. The convergence thresholds for geometry optimization were set at 2×10^{-5} Hartree (Ha), 2×10^{-2} Ha $Å^{-1}$ and 10^{-2} Å for energy, force and displacement, respectively. All geometry optimizations converged within 200 iterations.

Long-range vdW interactions were accounted for by semi-empirical correction via the Tkatchenko–Scheffler scheme[25]. The computed 1ADCu structure is close (<1.5% bond length and angle deviation, Supplementary Table 2) to the measured structure, which validates the computational method. Moreover, this method computed the bond dissociation energy of the diamantane dimer to be 75.3 kJ mol^{-1}, agreeing within 15% with the previously reported value[17] using hybrid functionals such as B3LYP-D[55] and M06-2X[56] that include long-range interactions. The Tkatchenko–Scheffler correction was intentionally turned off to compute the sterically favoured structures and their energies without contribution from vdW interactions (Supplementary Fig. 4).

Ab initio computations of the band structures were performed at the National Energy Research Scientific Computing Center (NERSC), using both the PBE functional[23] and HSE hybrid functional[32] and a plane-wave basis set implemented in Quantum Espresso[57]. The lattice constants and atom positions for both materials were taken from experimental data. We used a $4 \times 8 \times 4$ *k*-space grid for PBE calculations and a $1 \times 4 \times 1$ *k*-space grid for HSE calculations.

The effective carrier mass near the VBM and CBM is defined with a parabolic approximation:

$$m^* = \frac{(h/2\pi)^2 k^2}{2[E(k) - E_0]}$$

where h and E_0 are the Planck constant and energy at VBM/CBM respectively, and k is the wavevector along the G–Y direction. A weighted local fitting was used to determine m^*, with a Gaussian-form weight:

$$w = \exp\left[\frac{-(k-k_0)^2}{\sigma^2}\right]$$

where k_0 is the wavevector at VBM/CBM, and σ is taken to be 0.4.

Characterizations. X-ray photoelectron spectroscopy was recorded using a Versaprobe system (Physical Electronics) with an Al Kα (1486 eV) source in 10^{-5}-torr vacuum. Samples were prepared by pressing dry powders on degenerately doped silicon wafers. For scanning electron microscopy (SEM) imaging (Fig. 1b), crystals were lifted carefully from the interface and deposited on a silicon substrate. Excess solvent and a few drops of ethanol were wicked using absorptive paper and the crystals were allowed to dry in air. SEM micrographs were obtained on an FEI Magellan system with 1-kV acceleration voltage. To reduce charging artefacts, samples were sputter-coated with 5-nm Au. SEM imaging of the MOC vertical array (Fig. 5f) was performed at the same conditions without Au sputtering. The sample surface was tilted 60° relative to the electron beam. For AFM imaging (inset, Fig. 1b), cleaned and dried crystals were dispersed in IPA and spin-cast on a silicon wafer. AFM images were obtained on an Asylum Cypher ES system using non-contact mode and a Si probe.

Diffuse reflectance ultraviolet–visible absorption spectra were obtained on an Agilent Cary 6000i spectrometer equipped with a diffusive reflectance accessory. An ethanolic suspension of the crystals was drop-cast on a sapphire substrate, which was then laid on a white diffusive reflectance background with >99% reflectance. The optical bandgaps were determined by the intersection of the tangents of the baseline and the first absorption edge.

To measure the a.c. impedance of vertical MOC arrays, the MOC-embedded AAO membrane was first sonicated in IPA. Two electrodes consisting of 5-nm Ti and 200-nm Au were then evaporated on both sides of the AAO membrane. To measure the a.c. impedance of doped 1ADCu powder samples (Supplementary Fig. 10), ∼20 mg dry powders were filled in a quartz tube with 15-mm inner diameter, and two gold-plated stainless-steel disks were used as electrodes. a.c. impedance spectra were recorded using an impedance analyser (SP-200, Bio-Logic), with 50-mV peak-to-peak bias voltage in the frequency range of 1 Hz to 1 MHz.

The Nyquist plots were fitted with a nonlinear least-square fitting algorithm, implemented in Z-fit in the Bio-Logic EC-lab suite. All data points were equally weighted. The equivalent circuit for the vertically aligned MOC crystal arrays is shown in the inset of Fig. 5g. Axial resistivity of the MOCs were calculated by

$$\rho_{MOC} = \frac{R_{MOC} \times (\alpha A)}{d}$$

where ρ, A and d are the resistivity, cross-section of the electrode (0.7 cm^2) and thickness of the AAO membrane (60 μm), respectively. α is the filling ratio of the MOC crystals in the AAO membrane, and was determined by SEM to be ∼0.03%. The calculation yielded ρ_{MOC} of ∼100 Ω m and ∼300 Ω m for 1ADCu and 4DICu respectively.

The equivalent circuit for the randomly oriented MOC powder samples, shown in the inset of Supplementary Fig. 10, consists of two resistors (R_1, R_2), a capacitor (C_1) and a constant-phase element (Q_2). We attribute C_1 and R_1 to the capacitance/resistance of the inorganic core, while Q_2 and R_2 represent the transport through defects, grain boundaries and electrode barriers[58]. We found that this circuit model yielded the best fitting of the experimental data (Supplementary Fig. 10). The relative change of R_1 is plotted in Fig. 5h.

Data availability. The data supporting the findings of this study are available within the article and its Supplementary Information or from the authors. The crystallographic data have been deposited with the Cambridge Crystallographic Data Centre under CCDC-1512970 and 1512971. These data can be obtained free of charge from The Cambridge Crystallographic Data Centre via www.ccdc.cam.ac.uk/data_request/cif. The crystallographic data in CIF format are also available as Supplementary Data 1 and 2.

References

43. Tkachenko, B. A. *et al*. Functionalized nanodiamonds part 3: thiolation of tertiary/bridgehead alcohols. *Org. Lett.* **8,** 1767–1770 (2006).
44. Hohman, J. N. *et al*. Dynamic double lattice of 1-adamantaneselenolate self-assembled monolayerse on Au111. *J. Am. Chem. Soc.* **133,** 19422–19431 (2011).
45. Skrabalak, S. E., Wiley, B. J., Kim, M., Formo, E. V. & Xia, Y. On the polyol synthesis of silver nanostructures: glycolaldehyde as a reducing agent. *Nano Lett.* **8,** 2077–2081 (2008).
46. Stange, A. F., Klein, A., Klinkhammer, K.-W. & Kaim, W. Aggregation control of copper(I) thiolates through substituent size and ancillary chelate ligands: closely related mono-, di-, tri- and tetranuclear complexes. *Inorg. Chim. Acta* **324,** 336–341 (2001).
47. Eichhöfer, A. *et al*. Homoleptic 1-D iron selenolate complexes—synthesis, structure, magnetic and thermal behaviour of $^1_\infty$[Fe(SeR)$_2$] (R = Ph, Mes). *Dalt. Trans.* **40,** 7022–7032 (2011).
48. MacDiarmid, A. G. *et al*. The concept of 'doping' of conducting polymers: the role of reduction potentials [and discussion]. *Phil. Trans. R. Soc. A Math. Phys. Eng. Sci.* **314,** 3–15 (1985).
49. Bruker, *SAINT and SADABS* (Bruker AXS, 2007).
50. Kabsch, W. XDS. *Acta Crystallogr. D* **66,** 125–132 (2010).
51. Sheldrick, G. M. Crystal structure refinement with SHELXL. *Acta Crystallogr. C* **71,** 3–8 (2015).
52. Sheldrick, G. M. A short history of SHELX. *Acta Crystallogr. A* **64,** 112–122 (2008).
53. Dolomanov, O. V., Bourhis, L. J., Gildea, R. J., Howard, J. A. K. & Puschmann, H. OLEX2: a complete structure solution, refinement and analysis program. *J. Appl. Crystallogr.* **42,** 339–341 (2009).
54. McPhillips, T. M. *et al*. Blu-Ice and the Distributed Control System: software for data acquisition and instrument control at macromolecular crystallography beamlines. *J. Synchrotron Radiat.* **9,** 401–406 (2002).
55. Grimme, S. Accurate description of van der Waals complexes by density functional theory including empirical corrections. *J. Comput. Chem.* **25,** 1463–1473 (2004).
56. Zhao, Y. & Truhlar, D. G. The M06 suite of density functionals for main group thermochemistry, thermochemical kinetics, noncovalent interactions, excited states, and transition elements: two new functionals and systematic testing of four M06-class functionals and 12 other functionals. *Theor. Chem. Acc.* **120,** 215–241 (2008).
57. Giannozzi, P. *et al*. QUANTUM ESPRESSO: a modular and open-source software project for quantum simulations of materials. *J. Phys. Condens. Matter* **21,** 395502 (2009).
58. Okubo, T. *et al*. Crystal structure and carrier transport properties of a new semiconducting 2D coordination polymer with a 3,5-dimethylpiperidine dithiocarbamate ligand. *Chem. Commun.* **49,** 4316–4318 (2013).